Supporting information for:

Giant Enhancement of Photoluminescence Emission in WS_2-2D Perovskite Heterostructures

Arky Yang[1]*, Jean-Christophe Blancon[2]*, Wei Jiang[3], Hao Zhang[2], Joeson Wong[1], Ellen Yan[1], Yi-Rung Lin[1], Jared Crochet[2], Mercouri G. Kanatzidis[4], Deep Jariwala[1]**, Tony Low[3], Aditya D. Mohite[2]*** and Harry A. Atwater[1]***

*[1]California Institute of Technology, Pasadena, CA, 91125, USA.[2]Department of Chemical and Biomolecular Engineering, Rice University, Houston, TX 77005, USA. [3]Department of Electrical and Computer Engineering, University of Minnesota, Minneapolis, MN, 55455, USA. [4]Northwestern University, Evanston, IL, 60208, USA.*A. Yang and J. Blancon contributed equally to this work. **Currently at Department of Electrical and Systems Engineering, University of Pennsylvania, Philadelphia, PA 19104 USA.*

***Corresponding authors: Aditya Mohite (adm4@rice.edu), Harry Atwater (haa@caltech.edu)

1. Spatial variation of PL emission

Photoluminescence at different regions of 2L WS_2/ n=4 2DPVSK sample is shown in Supplementary Fig. 2a, corresponding to spots labeled in Supplementary Fig. 2b. Bare 2DPVSK shows varying emission intensity, likely due to differences in thickness and degree of degradation caused by the transfer process. Bare WS_2 also shows spatial variation in PL intensity despite Raman spectra that show the same number of layers. This might be attributed to variation in defect types/ densities in different regions of the material, as well as inhomogeneous interaction with the underlying substrate. Het-1 shows the highest emission among all heterostructure regions, in agreement with the PL mapping shown in MS Fig. 3b. This can be caused by a combination of variation on 2DPVSK quality, WS_2 defects, and interlayer interactions. The spatial inhomogeneity indicates that interface between TMDC and 2DPVSK layer plays an important role in the PL enhancement. More careful investigation and modeling of the interface is required to fully understand the origin of the PL enhancement.

2. Effect of spacer layer on 2L WS_2 PL emission

To study the potential dielectric screening effect that 2DPVSK may impose on 2L WS_2, control samples 2L WS_2/hBN/SiO_2/Si and 2L WS_2/butylammonium iodide(BAI)/SiO_2/Si were fabricated. WS_2/hBN heterostructure was obtained by dry exfoliation and transfer, while WS_2/BAI heterostructure was obtained by first spin-coating BAI solution (1mg/ml in DMF) onto SiO_2/Si substrate, followed by dry transfer of WS_2. Optical images of resulting heterostructures are shown in Supplementary Fig 7 a and b. Photoluminescence spectra of corresponding region are shown in

Supplementary Fig. 7c. Comparing to bare 2L WS_2, 2L WS_2/hBN heterostructure does not show enhanced PL intensity, but increased ratio between peak intensities of indirect and direct transition. This observation indicates that introducing similar spacer effect cannot explain the PL enhancement in 2L WS_2/2DPVSK heterostructure. 2L WS_2/BAI shows decreased PL emission as well as emergence of lower energy peak. This indicates that bare BA cation does not induce the PL enhancement. Comparing to BA in 2DPVSK, spin-coated BA is randomly oriented, which may enhance surface roughness and reduce WS_2 emission. Raman spectra (Supplementary Fig. 7d) of corresponding region do not show significant peak shift or change in intensity ratio between A^1_g and E^2_g peaks. Overall, simply shielding the effect from SiO_2 substrate on 2L WS_2 does not enhance PL of WS_2.

3. Optical characterizations on 1L WS_2/ n=3 2DPVSK heterostructure

An optical image of a 1L WS_2/ n=3 2DPVSK heterostructure is shown in Supplementary Figure 3a. In the Raman spectrum (Supplementary Figure 3b), a separation of 66 cm^{-1} between E^1_g and A^1_g vibration mode and higher intensity of E^1_g mode for 1L WS_2/n=3 2DPVSK heterostructure indicate a monolayer thickness of WS_2. Room temperature PL of WS2 and heterostructure is shown in Supplementary Figure 3c. The heterostructure experiences laser curing effect similar to 2L WS_2/n=4 2DPVSK heterostructure. Before curing, heterostructure exhibits 27 folds of enhancement of PL emission over WS_2. After curing, a broad peak at 1.71eV is observed in the heterostructure area, which shows 81 folds enhancement in overall integrated PL intensity. In comparison to the three peaks identified for 2L WS_2/n=4 2DPVSK sample, monolayer (1L) WS_2 shows only two emission features, one broad peak at 1.84eV and another narrow peak at 1.98eV (Supplementary Figure 3d). An overall 134-fold enhancement at an excitation power of 10μW was observed under low temperature, which is lower than what was observed for WS_2/n=4 2DPVSK sample. Reflection spectra (Supplementary Figure 3e) shows the presence of A exciton transition and B exciton of WS_2 in both WS_2 and heteorstructure region. Absorption at 1.98eV in all three regions corresponds to sharp peak at PL spectra.[3] PLE spectra (Supplementary Figure 3f) shows overall 250 times and 70 times enhancement of intensity on heterostructure comparing to bare n=3 2DPVSK and 1L WS_2. Specifically, peaks denoted as H_6 and H_8 are significantly enhanced in heterostructure, concommitent with the observed enhancement of H_6 and H_8 in 2L WS_2/n=4 2DPVSK heterostructure. Power dependence of heterostructure is shown in Supplementary Fig. 5. Main exciton peak at 2.00-2.01eV is denoted as H_1 and the shoulder at 1.99-2.00eV as H_0. Both of the peaks show near-linear dependence on excitation power density (Supplementary Fig. 4b), which confirms their excitonic nature. H_0 shoulder is likely defect-bound exciton confirmed with disappearance at room temperature due to thermal excitation. In contrast to H_0 in 2L WS_2/ n=4 2DPVSK heterostructure, neither of the peak and shoulder experiences observable peak shift with increasing power. Power dependence of FWHM of these two peaks show slight decrease with increasing power density, likely due to lower signal to noise ratio at lower excitation power.

Valence band position of n=3 2DPVSK is obtained from UPS measurements (Supplementary Figure 6a), and band alignment of n=3 2DPVSK and 1L WS_2 shows that 1L WS_2 and n=3 2DPVSK form a type II band alignment (Supplementary Figure 6b). Similar to 2L/n=4

heterostructure, the exciton 2s of n=3 2DPVSK is also in resonance with A exciton 1s of 1L WS_2, indicating possible channel for resonant energy transfer. 1L WS_2/n=3 2DPVSK heterostructure show less emission enhancement of WS2 on heterostructure comparing to bare WS2 (Supplementary Figure 3c). Mapping on n=3 2DPVSK exciton peak does not show the absence of 2DPVSK PL on the heterostructure, due to an overlap in emission wavelength of the WS_2 exciton and n=3 2DPVSK exciton (Supplementary Figure 6c). In contrast to the shorter lifetime of n=4 2DPVSK in heterostructure, almost identical lifetimes are observed in the n=3 heterostructure (Supplementary Figure 6d), and are close to the system resolution of our experimental setup.

Methods

Sample Preparation. 2D Perovskite bulk crystals with the composition $(BA)_2(MA)_5Pb_4I_{13}$ were synthesized as previously reported.[4] WS_2 bulk crystals were purchased from HQ Graphene. A schematic of the dry transfer process to fabricate TMD-2DPVSK heterostructure is shown in Supplementary Fig. 1. 285nm SiO_2/Si substrate (University Wafer) was cleaned with acetone and isopropanol using ultrasonication (15 min each), and subsequently subjected to oxygen plasma cleaning (5min, 100W, 300mTorr under O_2 flow). The bottom layer of the heterostructure (2DPVSK) was exfoliated directly onto the cleaned SiO_2/Si substrate using dicing tape (blue low tack roll, Semiconductor Equipment Corp). Top WS_2 layers were transferred using a viscoelastic dry transfer technique with a home-built setup in glovebox at room temperature without heating steps.[5] WS_2 was exfoliated with Scotch tape onto PF-20-X4 Gel Film from Gel-Pak supported by clear glass slides. Flakes are identified under optical microscope inside glovebox after each exfoliation.

Optical Characterization. Photoluminescence (PL), spatially-resolved PL, time-resolved photoluminescence (TRPL), photoluminescence emission (PLE), and optical reflection were performed with an in-lab-built confocal microscopy system.[3] The system focused a CW or 6-ps-pulsed laser close to the diffraction limit, and detected output light with a CCD camera (EMCCD 1024B) integrated with a spectrograph (Spectra-Pro 2300i). PL spectra are obtained with laser excitation at 550nm, with excitation intensity adjusted for different regions to obtain reasonable signal-to-noise ratio while preventing degradation of 2DPVSK. Spatial resolution of low temperature PL is achieved by rastering the laser beam onto sample surface with a fast steering mirror, and wavelength selection was achieved by reducing slit width before detection beam reaches Avalanche Photo-Diode (MPD-SPAD). TRPL was measured with a time correlated single photon counter (PicoHarp 300) and MPD-SPAD. All measurements mentioned above were carried out under vacuum (10^{-5}-10^{-6} torr) at liquid helium temperature (~7K). Raman and room temperature PL are measured in ambient condition using Renishaw M1000 Micro Raman Spectrometer System with 514nm laser excitation with 100x objective (spot size ~1μm). Room temperature PL map was extracted from hyperspectral map obtained by scanning over the sample using mechanical motor stage integrated into Renishaw system. All PL peak positions and FWHM were obtained from fitting of individual peaks using Gaussian function, and integration of the peaks gives corresponding PL intensity. Due to low intensity of H_2 peaks comparing to H_0 and H_1, intensity of H_2 peaks were extracted from Gaussian peak fitting of spectra subtracting a background of linear sections defined by valleys (Supplementary Fig. 8). Power dependent PL emission intensities are normalized by dividing the original intensity by integration time for comparison of intensity between heterostructure and WS_2 (Figure 3e). Raman peak positions are obtained from fitting with Voigt functions, calibrated with Si peak at 520cm^{-1}.

Ultraviolet photoelectron spectroscopy (UPS). Thick flakes were exfoliated onto gold substrate to expose clean surface right before UPS measurements. UPS measurements were performed using a Kratos AXIS Ultra spectrometer with a He I ultraviolet source (21.2 eV) at a pressure of 1×10^{-8} Torr in the analysis chamber. The photoelectron ejection vector was 90° with respect to the sample surface plane, the electron-collection lens aperture was set to a 55 μm spot size, and the analyzer pass energy was 5 eV. The instrument energy scale and work function were calibrated using clean Au, Ag, and Cu standards. Interceptions of linear fitting on high kinetic energy (KE) cutoff (Fermi edge) and low KE cutoff of the spectra gives the width of the binding energy (ΔE). The difference between ΔE and the He I source energy (21.22 eV) gives the binding energy of valence band maximum electrons referenced to the vacuum level.[6]

Transfer Matrix Calculation. Transfer matrix calculations were carried out in MATLAB with code designed according to methods described by Wong et al.[7,8] Refractive index(n) and absorbance(k) of 2D-PVSK and WS_2 are obtained from Guo et al.[9] and Li et al.[10], respectively. The n and k values of SiO_2 and Si are obtained from literature reports.[11,12] Infinite thickness was assumed as a realistic approximation for the Si substrate. Air-dielectric interface is defined as z=0. The thickness of the 2L WS_2 is determined to be 1.7nm from literature for typical bilayer WS_2.[13] The thickness of the n=4 2DPVSK is estimated to be 10nm from optical contrast.

Calculation method. The structural and electronic properties of the 2D perovskites (2DPVSK), transition metal dichalcogenides (TMD, WS_2), and their heterostructures were studied using first-principles methods based on density functional theory (DFT). We applied the generalized gradient approximation exchange-correlation potentials plus the projector augmented wave method for the electron-ion interaction for the calculations[14], as implemented in Vienna *ab initio* simulation package (VASP) code[15]. The heterostructures were built with 5×3 supercell of WS_2 on 2×2 supercell of 2DPVSK, after balancing the lattice mismatch and the size of the system given the limitation of the DFT calculation. A vacuum region of more than 15 Å was introduced between slabs to avoid the interaction between slabs. DFT-D3 method was applied to properly treat the van der Waals interaction between layers[16]. The dipole correctionswas applied to properly treat the dipole moment due to the formation of heterostructure[17]. An electric field is applied along the *z* direction of the multilayer WS_2 thin films with the dipole corrections applied to study the E-field effect. All self-consistent calculations were performed with a plane-wave cutoff of 400 eV. The geometric optimizations were carried out without any constraint until the force on each atom is less than 0.01 eV/ Å and the change of total energy per cell is smaller than 10^{-4} eV. The Brillouin zone k-point sampling was set with a $3 \times 3 \times 1$ Γ-centered Monkhorst-Pack grids. The charge transfer distribution was calculated by subtracting the charge of isolated WS_2 and 2DPVSK from that of their heterostructure. To get the change of the plane-averaged potential (PAP) profile due to the formation of the heterostructure, the PAP of isolated WS_2 and 2DPVSK were first aligned with and then subtracted from that of their heterostructure.

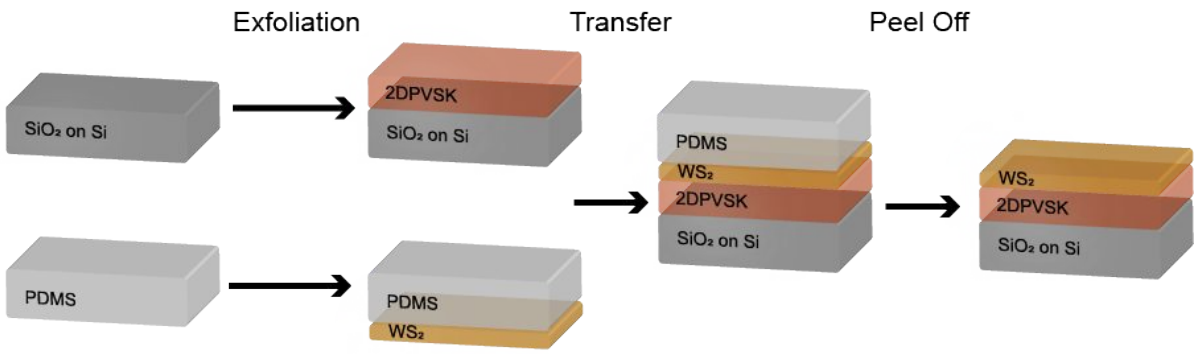

Supplementary Figure 1. Schematics of exfoliation and dry transfer process for heterostructure fabrication. The whole process is carried out inside a glovebox under microscope objective with remote-controlled mechanical manipulator.

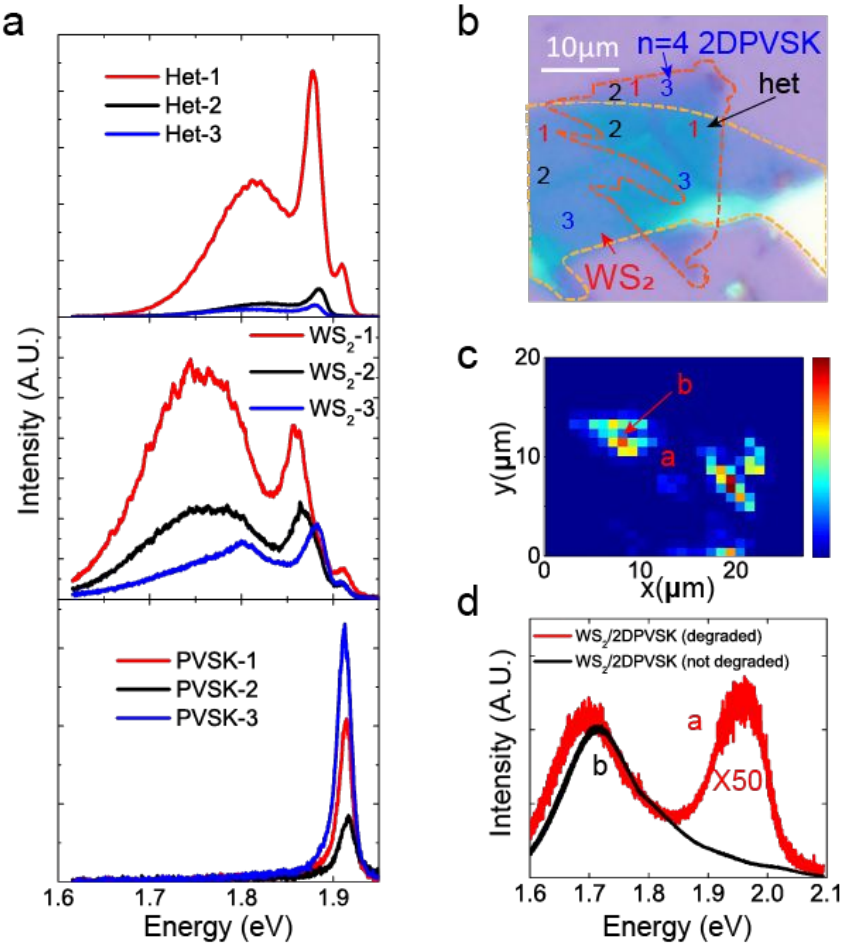

Supplementary Figure 2. (a) PL emission spectra at different regions of sample taken at 900 W/cm^2 (WS_2) and 5W/cm^2 (heterostructure and 2DPVSK) at 550nm laser excitation. Vertical

scales of the three subplots are arbitrarily chosen and not the same. (b) Optical image of the sample with spots labeled correspondingly. (c) Integrated PL intensity map over 1.6-1.7 eV, measured at 514nm 3kW/cm^2 laser excitation and integration time of 3s per point. (d) PL spectra extracted from the map at heterostructure where 2DPVSK has degraded (point a) and not degraded (point b).

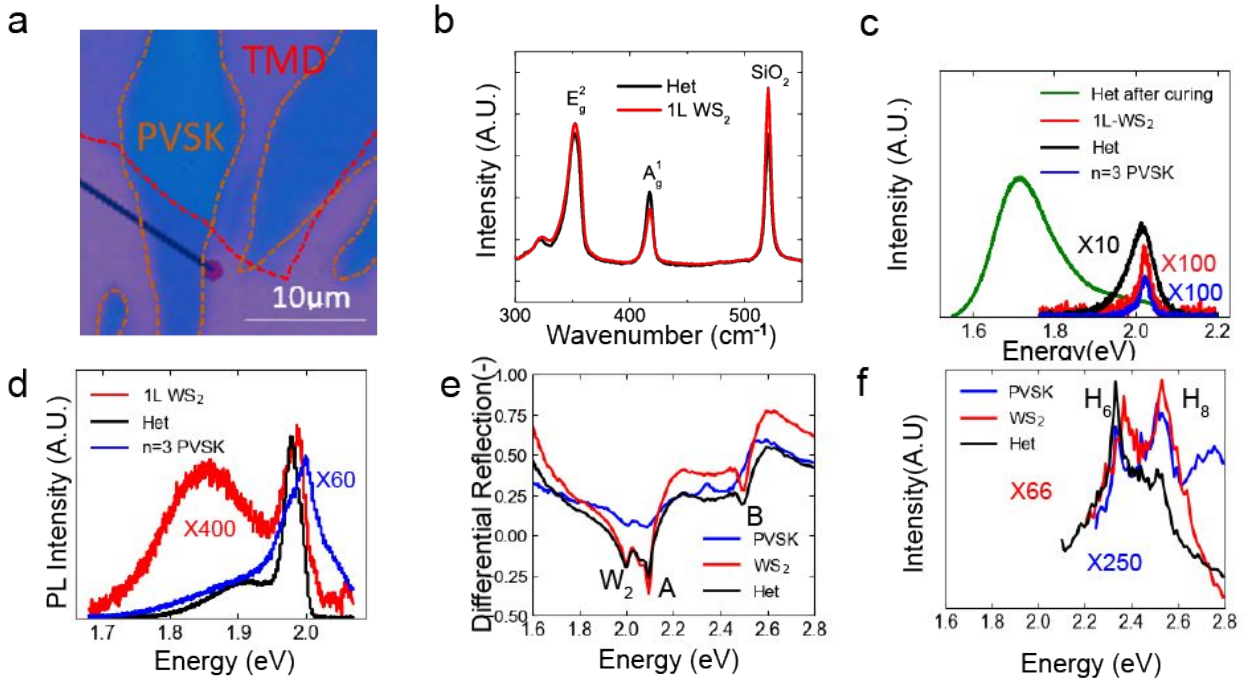

Supplementary Figure 3. Optical measurements on 2L WS_2/n=3 2DPVSK heterostructure. (a) Optical image of 2L WS_2/n=3 2DPVSK heterostructure on SiO_2/Si substrate. (b) Raman spectra of the bare WS_2 and the heterostructure. (c) Room temperature photoluminescence spectra taken with 514 nm laser excitation at 3kW/cm^2. (d) PL emission of 1L WS_2/n=3 2DPVSK heterostructure at 7K with 561nm laser excitation at 1kW/cm^2 before interface curing. Corresponding reflection (e) and photoluminescence excitation PLE (f).

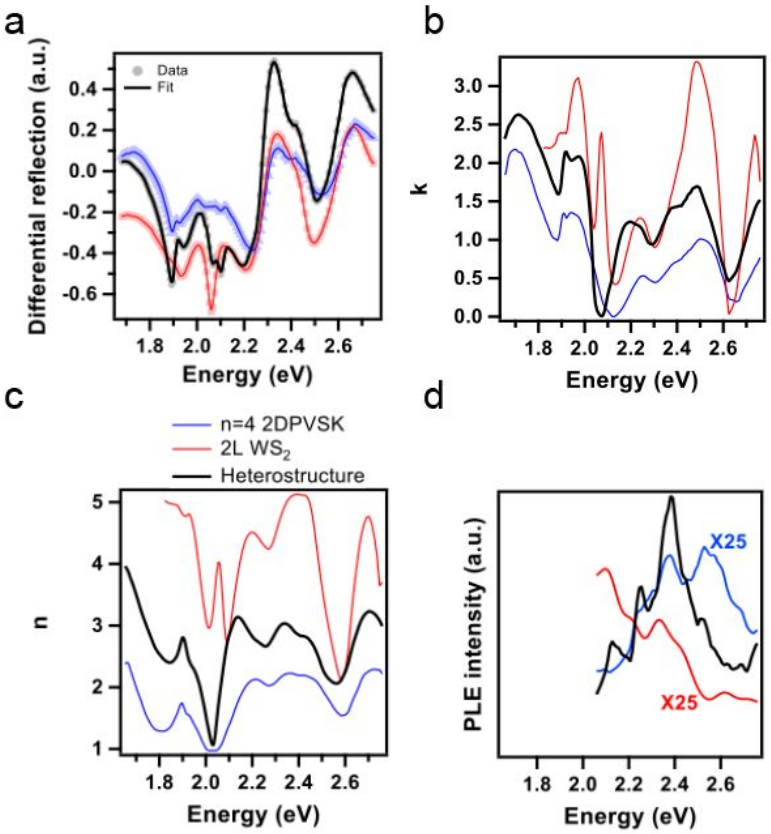

Supplementary Figure 4. Optical constant fitting on differential reflection spectra of 2L WS_2/ n=4 2DPVSK sample. (a) Experimental differential reflection spectra and fitting line. (b) Extinction coefficient and (c) refractive index obtained from fitting. (d) Experimental PLE spectra measured at 600nW. The complex refractive index were obtained by Kramer's-Kronig constrained fitting of the differential reflection spectra. The spectral dependence of real part of refractive index n, can be derived from imaginary part k using Kramer's-Kronig relation, under the assumption that the contribution beyond the spectral range can be represented by one additional constant. Using this relation, we derived the best n and k couple fitting the experimental data.

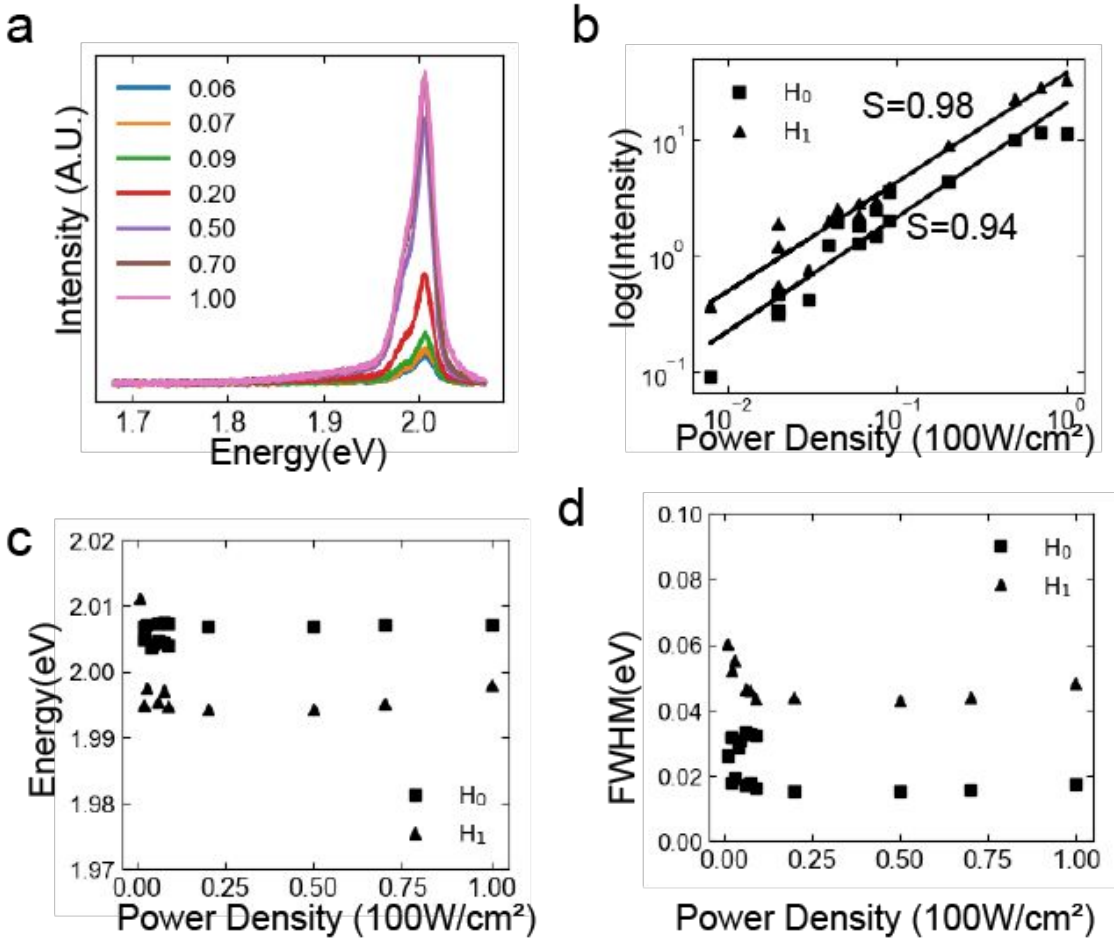

Supplementary Figure 5. Power dependence of PL emission of 1L WS_2/n=3 2DPVSK at 7K. (a) PL spectra of heterostructure taken at different incident laser power. Power dependence of (b) integrated PL intensity and (c) peak position of the photoemission transitions of the heterostructure. (d) Corresponding power dependent of the FWHM.

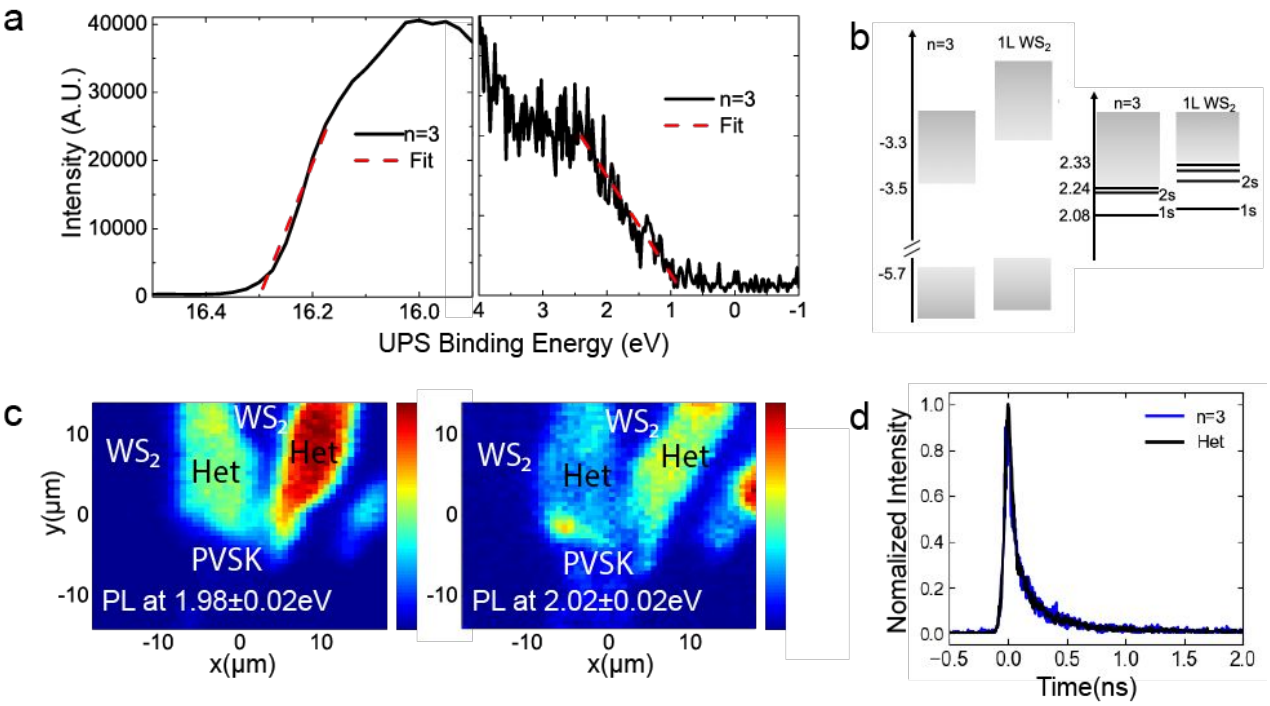

Supplementary Figure 6. (a) UPS spectra for the 1L WS_2/n=3 heterostructure at low KE region with linear fitting at the edge (left) and high KE region with linear fitting at Fermi edge (right). (b) (Left)Corresponding band positions of n=3 2DPVSK and 1L WS_2, with grey boxes indicating conduction and valance band. (Right) Energy diagram in the excitonic picture for the bare n=3 2DPVSK and the bare WS_2 taken from previous reports.[9,10] Black lines indicate the exciton Rydberg series. (c) Map of photoluminescence at low temperature corresponding to Supplementary Fig. 3d. (d) Time resolved PL of n=3 PVSK exciton peak and heterostructure at low temperature corresponding to Supplementary Fig. 3d. Both samples show PL decay on par or faster with the resolution of our TRPL system.

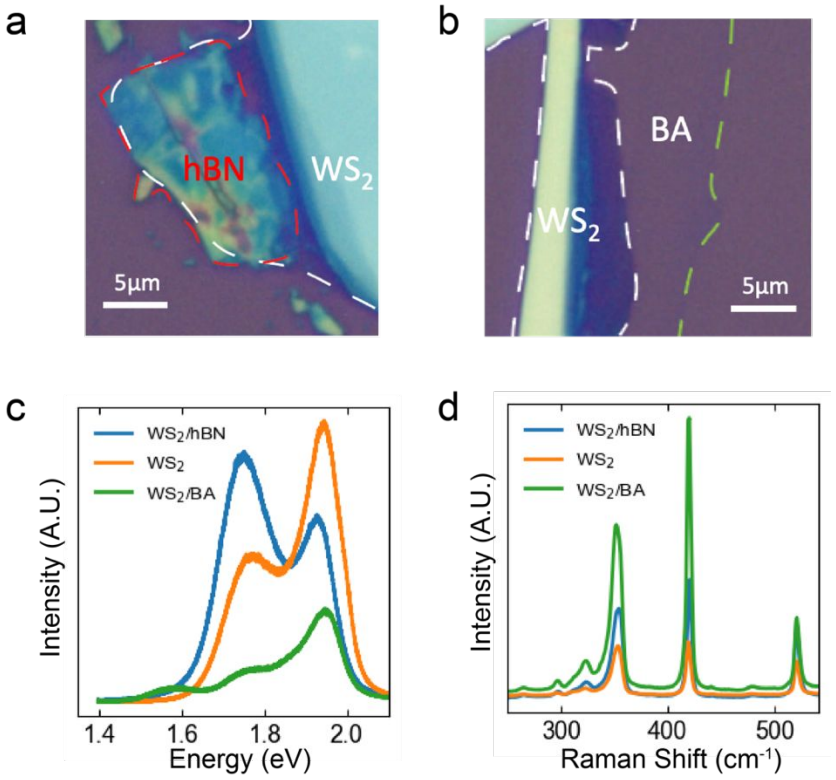

Supplementary Figure 7. (a) Optical image of 2L WS_2 on hBN heterostructure. b) Optical image of 2L WS_2 on spin-coated BAI heterostructure. (c) PL emission of three regions taken at 514nm excitation under room temperature and ambient atmosphere. (d) Raman spectra of corresponding regions under the same condition.

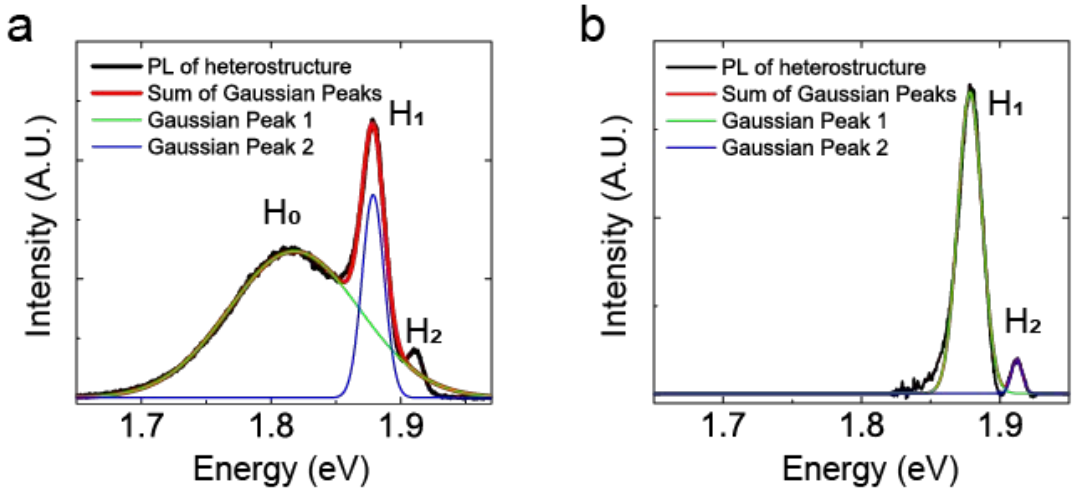

Supplementary Figure 8. Example plot of Gaussian peak fitting for power dependence analysis. The spectra were taken on heterostructure at excitation power density of 65W/cm^2. (a) H_0 and H_1 are fitted from the raw data using two Gaussian peaks. (b) H_2 is fitted from raw data subtracted with sections of linear background defined by valleys between peaks.

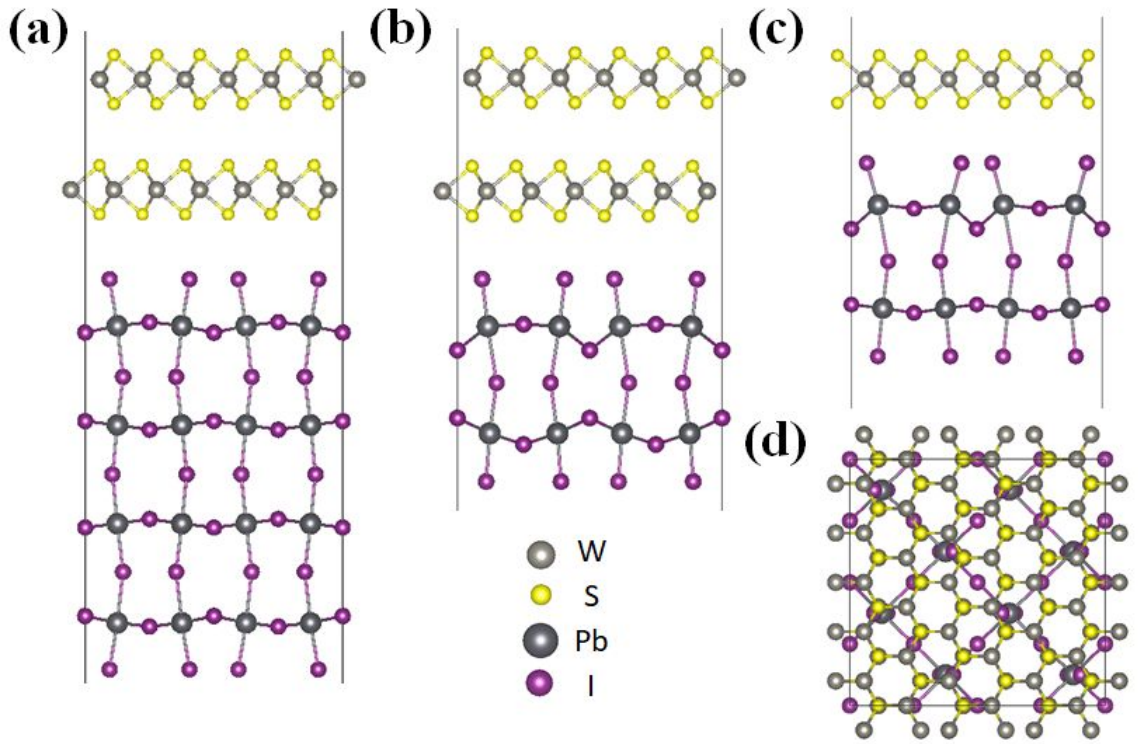

Supplementary Figure 9. Heterostructures of WS_2 and 2DPVSK with different thickness. Side view of heterostructure of (a) 2L WS_2 and n=4 2DPVSK, (b) 2L WS2 and n=2 2DPVSK, and (c) 1L WS2 and n=2 2DPVSK. (d) Top view of the heterostructure.

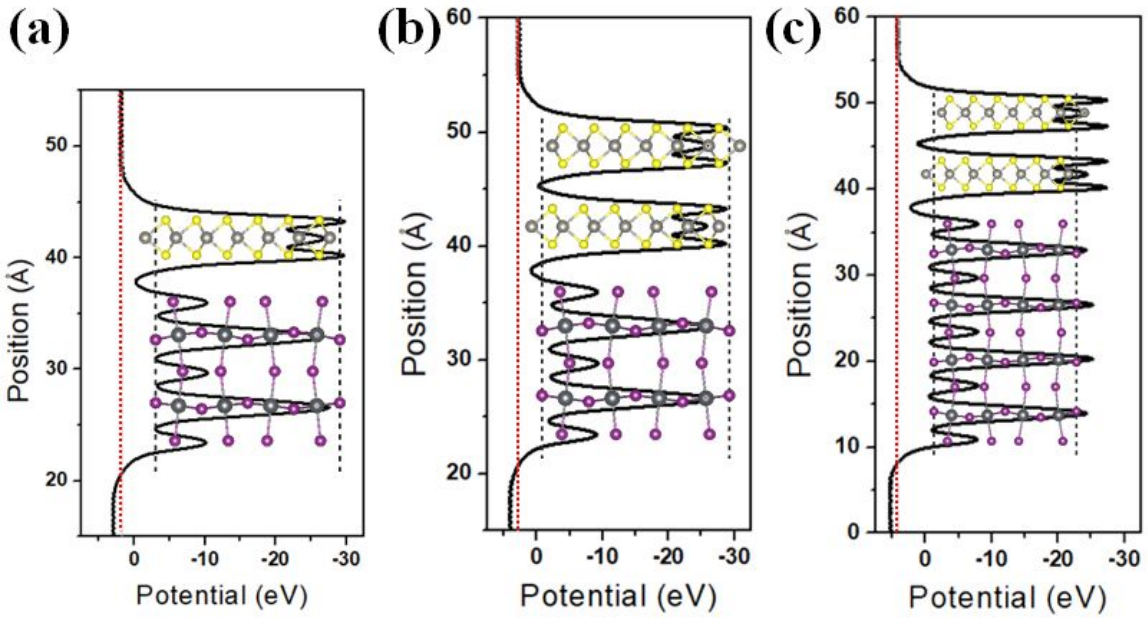

Supplementary Figure 10. Plane-averaged potential (PAP) profiles of heterostrutures. PAP profiles for (a) 1L WS_2/n=2 2DPVSK, (b) 2L WS_2/n=2 2DPVSK, and (c) 2L WS_2/n=4 2DPVSK all show the formation of dipole moment.

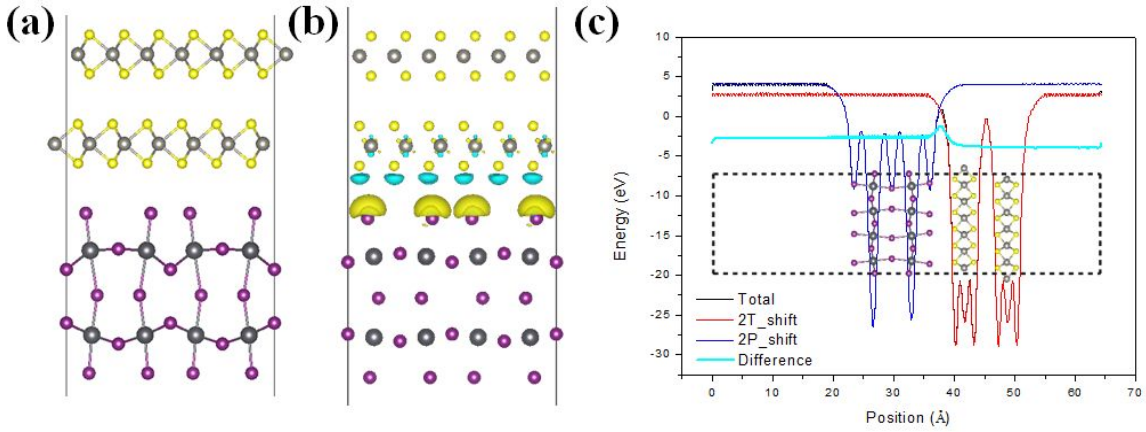

Supplementary Figure 11. Charge transfer and dipole moment of the 2L WS_2/n=2 2DPVSK. (a) and (b) The structure and the charge transfer of the system due to the formation of heterostructure. Yellow and blue color denote the electron and hole accumulation, indicating the charge transfer from 2DPVSK to 2L WS_2. (c) The plane average potential profile of heterostructure (Total, black), 2L WS2 (2T_shift, red), n=2 2DPVSK (2P_shift, blue), and the difference due to the formation of the heterostructure (Difference, Cyan).

References

(1) Fang, H. H.; Yang, J.; Tao, S.; Adjokatse, S.; Kamminga, M. E.; Ye, J.; Blake, G. R.; Even, J.; Loi, M. A. Unravelling Light-Induced Degradation of Layered Perovskite Crystals and Design of Efficient Encapsulation for Improved Photostability. *Adv. Funct. Mater.* **2018**, *28* (21).

(2) Zhao, W.; Ghorannevis, Z.; Chu, L.; Toh, M.; Kloc, C.; Tan, P.-H.; Eda, G. Evolution of Electronic Structure in Atomically Thin Sheets of WS2 AndWSe2. *ACS Nano* **2013**, *7* (1), 791–797.

(3) Blancon, J.-C.; Tsai, H.; Nie, W.; Stoumpos, C. C.; Pedesseau, L.; Katan, C.; Kepenekian, M.; Soe, C. M. M.; Appavoo, K.; Sfeir, M. Y.; et al. Extremely Efficient Internal Exciton Dissociation through Edge States in Layered 2D Perovskites. *Science.* **2017**, 355(6331), 1288-1292.

(4) Stoumpos, C. C.; Cao, D. H.; Clark, D. J.; Young, J.; Rondinelli, J. M.; Jang, J. I.; Hupp, J. T.; Kanatzidis, M. G. Ruddlesden-Popper Hybrid Lead Iodide Perovskite 2D Homologous Semiconductors. *Chem. Mater.* **2016**, *28* (8), 2852–2867.

(5) Castellanos-Gomez, A.; Buscema, M.; Molenaar, R.; Singh, V.; Janssen, L.; van der Zant, H. S. J.; Steele, G. A. Deterministic Transfer of Two-Dimensional Materials by All-Dry Viscoelastic Stamping. *2D Mater.* **2014**, *1* (1), 11002.

(6) Chun, W. J.; Ishikawa, A.; Fujisawa, H.; Takata, T.; Kondo, J. N.; Hara, M.; Kawai, M.; Matsumoto, Y.; Domen, K. Conduction and Valence Band Positions of Ta2O5, TaOn, and Ta3N5

by UPS and Electrochemical Methods. *J. Phys. Chem. B* **2003**, *107* (8), 1798–1803.

(7) Pettersson, L. A. A.; Roman, L. S.; Inganäs, O. Modeling Photocurrent Action Spectra of Photovoltaic Devices Based on Organic Thin Films. *J. Appl. Phys.* **1999**, *86* (1), 487–496.

(8) Wong, J.; Jariwala, D.; Tagliabue, G.; Tat, K.; Davoyan, A. R.; Sherrott, M. C.; Atwater, H. A. High Photovoltaic Quantum Efficiency in Ultrathin van Der Waal s Heterostructures. *ACS Nano* **2017**, *11* (7), 7230–7240.

(9) Guo, P.; Huang, W.; Stoumpos, C. C.; Mao, L.; Gong, J.; Zeng, L.; Diroll, B. T.; Xia, Y.; Ma, X.; Gosztola, D. J.; et al. Hyperbolic Dispersion Arising from Anisotropic Excitons in Two-Dimensional Perovskites. *Phys. Rev. Lett.* **2018**, *121* (12), 127401.

(10) Li, Y.; Chernikov, A.; Zhang, X.; Rigosi, A.; Hill, H. M.; Van Der Zande, A. M.; Chenet, D. A.; Shih, E. M.; Hone, J.; Heinz, T. F. Measurement of the Optical Dielectric Function of Monolayer Transition-Metal Dichalcogenides: MoS_2, $MoSe_2$, WS_2, and WSe_2. *Phys. Rev. B - Condens. Matter Mater. Phys.* **2014**, *90* (20), 1–6.

(11) Marcos, L. V. R.; Larruquert, J. I.; Méndez, J. A.; Aznárez, J. A. Self-Consistent Optical Constants of SiO2 and Ta2O5 Films. *Opt. Mater. Express* **2016**, *6* (11), 3622–3637.

(12) Schinke, C.; Christian Peest, P.; Schmidt, J.; Brendel, R.; Bothe, K.; Vogt, M. R.; Kröger, I.; Winter, S.; Schirmacher, A.; Lim, S.; et al. Uncertainty Analysis for the Coefficient of Band-to-Band Absorption of Crystalline Silicon. *AIP Adv.* **2015**, *5* (6), 67168.

(13) Chen, K.; Wan, X.; Wen, J.; Xie, W.; Kang, Z.; Zeng, X.; Chen, H.; Xu, J.-B. Electronic Properties of MoS_2–WS_2 Heterostructures Synthesized with Two-Step Lateral Epitaxial Strategy. *ACS Nano* **2015**, *9* (10), 9868–9876.

(14) G. Kresse and D. Joubert, *Phys. Rev. B* **59**, 1758 (1999).

(15) G. Kresse and J. Hafner, *Phys. Rev. B* **47**, 558 (1993).

(16) S. Grimme, J. Antony, S. Ehrlich, and S. Krieg, *J. Chem. Phys.* **132**, 154104 (2010).

(17) G. Makov and M.C.Payne, *Phys. Rev. B* **51**, 4014 (1995).